Research Square

Preprints are preliminary reports that have not undergone peer review.
They should not be considered conclusive, used to inform clinical practice,
or referenced by the media as validated information.

Thermally reconfigurable Rubik's-cube-inspired V–VO_2 hyperbolic metamaterial absorber for dual-band absorption and spectral coding

Mengxuan Wu

24s030027@stu.hit.edu.cn

Harbin Institute of Technology

Xuefeng Wang

Harbin Institute of Technology

Shuai Guo

Harbin Institute of Technology

Pengfei Li

Harbin Institute of Technology

Research Article

Keywords: Hyperbolic metamaterial absorber, vanadium dioxide, dual-band absorption, IFF

Posted Date: October 22nd, 2026

DOI: https://doi.org/10.21203/rs.3.rs-11047593/v1

License: This work is licensed under a Creative Commons Attribution 4.0 International License.
Read Full License

Additional Declarations: No competing interests reported.

Thermally reconfigurable Rubik's-cube-inspired V–VO_2 hyperbolic metamaterial absorber for dual-band absorption and spectral coding

Mengxuan Wu*, Xuefeng Wang, Shuai Guo *, Pengfei Li *

[a]*School of Science, Department of Optoelectronic Science, Harbin Institute of Technology at Weihai, Weihai, 264209, P.R. China*

Abstract

Microwave absorbers serve key functions in stealth, camouflage, and antenna systems. Extending the absorption bandwidth while maintaining polarization and angular stability remains challenging. Given this situation, a thermally reconfigurable V–VO_2 hyperbolic metamaterial absorber is proposed using nonlinearly graded multilayer pyramids. By using frequency–size mapping to determine the layer dimensions, the K- and Ka-band units achieve absorptance above 96% and 98%, respectively. To extend the absorption bandwidth, a Rubik's-Cube-inspired symmetric configuration is developed, achieving absorptance above 80% over 16–40 GHz while maintaining stable broadband absorption at incidence angles up to 50° and reducing the polarization sensitivity introduced by the adjacent arrangement of the two units. Owing to the thermally induced phase transition of VO_2, independent thermal switching of the K and Ka band units produces four distinguishable spectral states, enabling 2-bit coding in a dual-band metamaterial array. This work provides a design route to broadband absorption and thermal reconfigurability, with potential for backscatter-assisted, semi-passive identification friend or foe applications.

Keywords: Hyperbolic metamaterial absorber, vanadium dioxide, dual-band absorption, IFF

1. Introduction

Electromagnetic absorbers are widely used for stealth, camouflage, antenna, sensing, and imaging, where reflection must be suppressed over specified frequency and angular ranges[1-6]. Metamaterial is artificial structured material that enables its electric and magnetic responses to be engineered through subwavelength structures[2, 3, 7]. Metamaterial absorbers often consist of metallic and dielectric components. The metallic ground plane suppresses transmission, while the incident wave couples to resonant modes supported by the metal–dielectric structure, allowing electromagnetic energy to be dissipated through dielectric and metallic ohmic losses[3, 8, 9].

However, these resonant modes typically produce strong absorption only near their resonance frequencies, resulting in narrow absorption bands and making broadband absorption challenging [7-13]. Existing strategies include combining differently sized resonators, stacking patterned layers, introducing resistive films, and grading tapered structures. For example, At optical frequencies, Cui et al. obtained absorptance above 95% over an ultrabroad band by using a sawtooth anisotropic metamaterial slab, in which slow-light modes were localized at different vertical positions[7]. Ding et al. realized greater than 90% absorption from 7.8 to 14.7 GHz by vertically stacking differently sized resonators[8]. Tapered hyperbolic-metamaterial arrays subsequently connected multiple slow-light modes into a broadband response[9], and the integration of two differently sized tapered waveguides further extended microwave absorption from 2.3 to 40 GHz while retaining polarization and angular robustness[10]. However, these approaches often increase structural complexity or require extensive parameter optimization, motivating a more systematic design based on the relationship between layer dimensions and absorption frequency.

This study targets continuous absorption across the K to Ka frequency region which occupy 18–25and 25–40 GHz, respectively. K-band systems have been investigated for compact short-range radar and security imaging [14], whereas the shorter wavelengths and wider available bandwidths of the Ka band can support compact apertures and improved resolution, although atmospheric and rain attenuation must be considered [15]. Combining these adjacent bands provides a broad operating range and two spectrally distinguishable response regions. Reconfigurability further enables these responses to carry information[16, 17]. Conventional cooperative identification friend or foe (IFF) systems rely on active interrogation and transponder replies[18, 19], whereas passive or semi-passive backscatter systems encode information in controllable scattering signatures without requiring a dedicated high-power radio-frequency transmitter [20-23]. Vanadium dioxide (VO_2) is suitable for generating such signatures because its insulator-to-metal transition produces a large and reversible change in electrical conductivity, enabling thermally switchable metamaterial responses [13, 24-27]. Although ultrafast switching has been demonstrated in nanoscale VO_2 devices [26, 28-30], the switching performance of a macroscale thermal absorber depends on its geometry and thermal-control system. The present work therefore evaluates the electromagnetic feasibility of VO_2-based spectral coding without claiming a complete experimentally validated IFF system.

In this study, we propose a thermally reconfigurable hyperbolic metamaterial design for dual-band absorption and IFF application. The proposed absorber consists of alternating vanadium (V) and VO_2 layers arranged in a pyramidal structure with nonlinearly varying lateral dimensions and is designed to operate across the K and Ka bands. First, the single band absorber units are constructed using the nonlinearly graded pyramidal profile, which reduces the absorption fluctuations associated with conventional linearly graded hyperbolic pyramids. This

optimized design achieves an above 98% absorption in Ka band and 96% absorption in K band. Second, the two absorber units are placed adjacent to each other to broaden the absorption bandwidth, and their electromagnetic-field distributions are analyzed to clarify the absorption mechanism. To further reduce the polarization sensitivity introduced by the linear arrangement of the two units, a Rubik's-Cube-inspired plus-shaped configuration is developed, achieving absorptance above 80% over 16–40 GHz while maintaining stable absorption at oblique incidence angles from 0° to 50°. Owing to the thermally induced phase transition of VO_2, the absorber exhibits a clear spectral contrast between its insulating and metallic phases. Therefore, the plus-shaped configuration can be periodically repeated to form a dual-band metamaterial array for thermally reconfigurable coding. The proposed VO_2-based dual-band metamaterial absorber shows potential for stealth and passive IFF applications.

2. Design and simulation method

The proposed VO_2 -based metamaterial absorber is designed and constructed on the basis of conventional hyperbolic metamaterial.

Hyperbolic metamaterials are characterized by principal components of the permittivity tensor with opposite signs over a certain frequency range. For a uniaxial medium with its optical axis along the *z*-direction, the permittivity tensor is

$$\epsilon = \begin{pmatrix} \epsilon_{\perp} & 0 & 0 \\ 0 & \epsilon_{\perp} & 0 \\ 0 & 0 & \epsilon_{\parallel} \end{pmatrix}, \tag{1}$$

where $\varepsilon_{\perp}$ and $\varepsilon_{/\!/}$ denote the permittivity components perpendicular and parallel to the optical axis, respectively. Hyperbolic dispersion occurs when $\varepsilon_{\perp}>0$, $\varepsilon_{/\!/}<0$ or $\varepsilon_{\perp}<0$, $\varepsilon_{/\!/}>0$. The corresponding dispersion relation derived from Maxwell's equations is

$$\frac{k_x^2 + k_y^2}{\epsilon_{\parallel}} + \frac{k_z^2}{\epsilon_{\perp}} = \frac{\omega^2}{c^2}, \tag{2}$$

where k_x, k_y and k_z are the wave-vector components, ω is the angular frequency, and c is the speed of light in vacuum. When all principal permittivity components are positive, the isofrequency surface is spherical or ellipsoidal. In contrast, opposite signs produce an open hyperbolic surface that supports high-wave-vector bulk modes and enables subwavelength field manipulation. Specifically, $\varepsilon_{\perp}>0$, $\varepsilon_{/\!/}<0$ produces a one-sheet hyperboloid, whereas $\varepsilon_{\perp}<0$, $\varepsilon_{/\!/}>0$ produces a two-sheet hyperboloid[31].

By exploiting the slow-light waveguide effect, hyperbolic metamaterials can achieve ultrabroadband absorption within a compact structure. In hyperbolic metamaterials, slow-light

waveguiding can arise from resonances and multiple scattering, where localized resonances reduces the effective group velocity v_g and prolongs the interaction of incident wave with the lossy material, thereby enhancing electromagnetic absorption.[32]

The absorptance of the structure is expressed as

$$A = 1 - T - R, \tag{3}$$

where A, T, and R denote the absorptance, transmittance, and reflectance, respectively. If a PEC substrate is used, the transmittance can be considered nearly zero within the absorption frequency range, which means $T \approx 0$. Therefore, the absorptance can be simplified as

$$A = 1 - R. \tag{4}$$

After being reflected by the bottom PEC substrate, the incident wave undergoes multiple reflections at the interfaces within the multilayer hyperbolic structure. Interference among the reflected components suppresses the overall reflection, while the electromagnetic energy coupled into the structure is dissipated through dielectric and metallic ohmic losses. Because the PEC substrate blocks transmission, the reduced reflection results in high absorption. Resonant elements with different dimensions produce absorption peaks at different frequencies. By adjusting the element dimensions, these peaks can be distributed across the target frequency range. When adjacent peaks have sufficient bandwidth and overlap spectrally, they merge to form a continuous broadband absorption response[33].

To objectively compare absorbers operating in different frequency ranges, the relative absorption bandwidth (RAB) is defined as

$$\mathrm{RAB} = \frac{\Delta f}{f_c} \times 100\%, \tag{5}$$

where Δf is the frequency range over which the absorptance exceeds a specified threshold, such as 80%, and f_c is the arithmetic mean of its lower and upper frequency. By normalizing the absolute bandwidth to the center frequency, RAB enables comparison across different operating bands[8].

3. Results and Discussion

Conventional hyperbolic metamaterials commonly adopt a pyramidal geometry formed by alternately stacking metal and dielectric layers with linearly varying lateral dimensions. Although such structures can provide broadband absorption, their absorption spectra often exhibit pronounced fluctuations. In this study, we propose a metal V–dielectric VO_2 alternating

multilayered structure with nonlinear lateral dimensions (nonlinearly varying layer dimensions), as illustrated in Figure 1(a). The lateral dimensions of the bottom and top layers of the pyramid are denoted by l_1 and l_2 respectively, which correspond to the low and high frequency boundaries of the absorption band. The whole pyramid is placed on a PEC substrate with a thickness of t; the thicknesses of the VO_2 and V layers are t_s and t_m respectively. The resulting unit cell is periodically arranged with a period of p. The PEC substrate suppresses transmission, the lossy dielectric dissipates electromagnetic energy, and the metallic layers support resonant currents.

First, fix a random lateral layer dimension l and optimize the layer thicknesses to t_s and t_m determine the maximal absorption, as shown in Figure S1(a) and (b). A parameter sweep of l from l_1 to l_2 is then performed with the optimal t_s and t_m to establish the mapping between the layer dimension and the frequencies corresponding to the absorption peaks as shown in Figure S1(c). Plot the absorption frequency-layer length heating map as presented in the upper-left insets of Figure 1 (b) and (c), the absorption peak frequency-length appears to be a bright line follow a nonlinear trajectory ($y = a \cdot x^b$). This finding indicates that the conventional linear variation in layer dimensions leads to a mismatch between the spectral spacings of adjacent absorption peaks, resulting in noticeable fluctuations across the absorption band.

The resulting nonlinear relationship is used to construct the stacking profiles illustrated in the lower-left insets of Figure 1 (b) and (c). The geometrical parameters of the Ka-band unit in Figure 1 (b) are l_1=2.0506 mm, l_2=1.2993 mm, t_s=0.06 mm and t_m=0.01 mm. Those of the K-band unit in Figure 1 (c) are l_1=2.7792 mm, l_2=2.0666 mm, t_s=0.75 mm and t_m=0.01 mm. Both unit cells have a period of p=3 mm and a PEC substrate thickness of t=0.05mm. Frequency-domain simulations are performed using CST Studio Suite, and the resulting absorption spectra are shown in the right panels of Figure 1 (b) and (c). From the figure it can be deducted that Ka band reached above 98% absorption and K band reached above 96% absorption. Compare the nonlinear pyramidal design to conventional design in Ka band unit, the fluctuations across the absorption band are clearly reduced, increasing the absorption from 94% to 98%. The comparison is plotted in Figure S1 (d).

To further broaden the absorption bandwidth, the two absorber units are placed side by side along the x-direction as displayed in Figure 1 (d). This linear arrangement breaks the rotational symmetry of the overall structure in the x-y plane, resulting in different electromagnetic responses to electric fields polarized along different directions. The absorption spectra of the combined structure are therefore simulated under TE- and TM-polarized incidence wave, as shown in Figure 1 (e). The TM-polarized wave produces both stronger absorption and a wider effective absorption bandwidth than the TE-polarized wave, indicating a distinct polarization-dependent response. To examine the difference, the surface current distributions under the two polarizations are compared, as shown in Figure S2 (a) and (b). Under TE-polarized incidence,

the electric field is oriented along the y-direction, inducing relatively weak surface currents predominantly parallel to the y-axis. These currents are largely confined within the individual K- and Ka-band units. In contrast, under TM-polarized incidence, the electric field is oriented along the x-direction, parallel to the arrangement direction of the two units. Consequently, stronger surface currents are induced along the x-direction, indicating enhanced electromagnetic coupling between the K- and Ka-band units. Moreover, clear oppositely directed surface currents are observed on adjacent metallic layers, forming well-defined current loops and supporting a stronger layer-to-layer resonant response. These current characteristics indicate that the TM-polarized wave interacts more strongly with the combined structure, consistent with its higher absorption and broader effective absorption bandwidth.

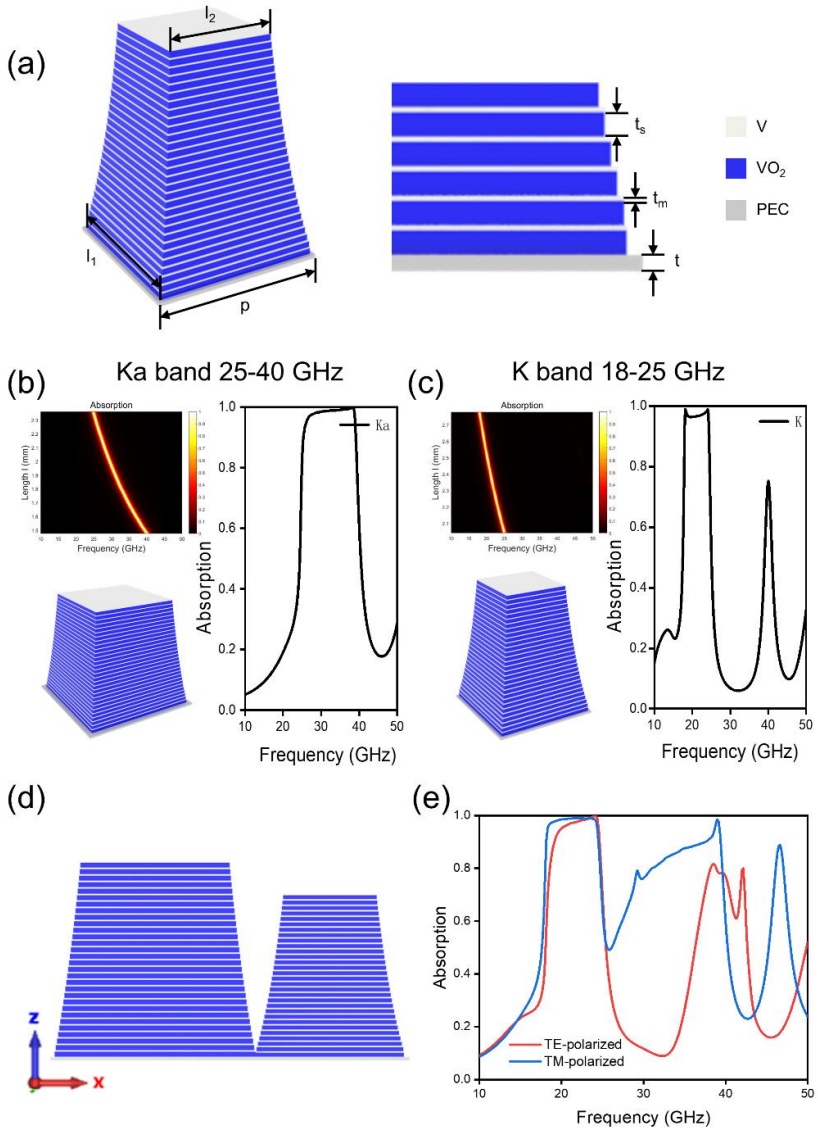

Figure 1. Design and absorption characteristics of the nonlinearly graded V–VO_2 hyperbolic absorber. (a) Schematic of the V–VO_2 pyramidal unit cell and its geometrical parameters. (b) Dimension-dependent absorptance map, fitted stacking profile, and simulated absorption

spectrum of the Ka-band unit. (c) Corresponding results for the K-band unit. (d) Adjacent combination of the K- and Ka-band units. (e) Absorption spectra of the combined structure under TE- and TM-polarized incidence wave.

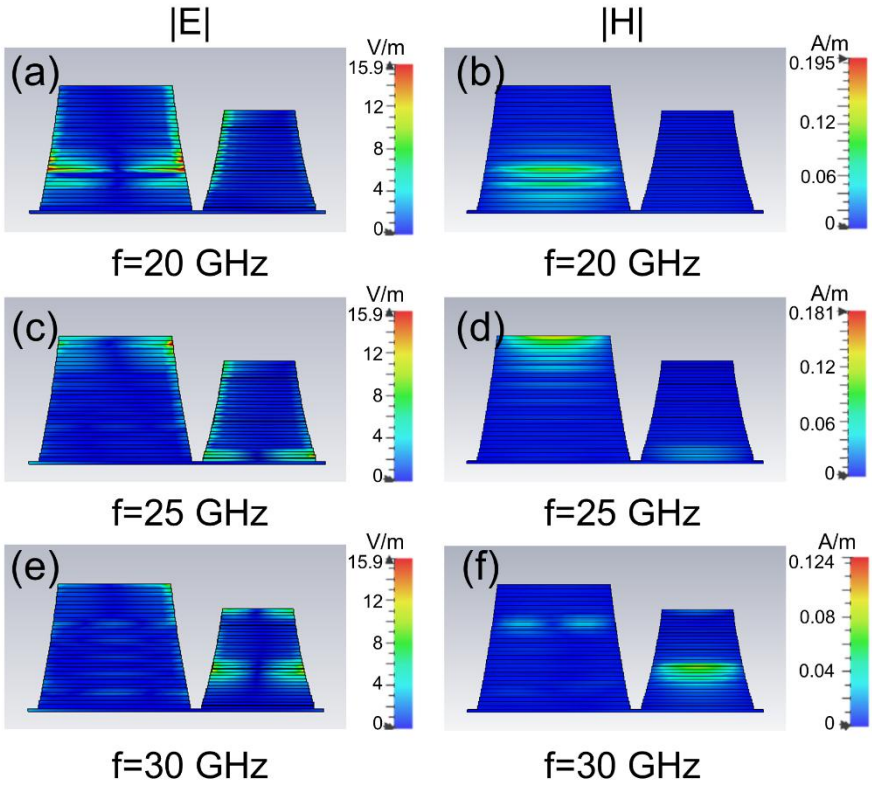

Figure 2 Obtained simulation results of the electric (a) (c) (e) and magnetic (b) (d) (f) magnitude distribution under three representative frequencies 20, 25, and 30 GHz.

Figure 2 presents the electric and magnetic field distributions at three representative frequencies (20, 25, and 30 GHz) to help provide insight into the physical mechanism behind the absorption. 20 GHz represents the magnitude distribution in K band, whereas 30 GHz corresponds to the Ka band and 25 GHz to both bands. These field distributions reveal a frequency-dependent shift of the dominant field localization from the lower to the upper layers of the K-band element and subsequently to the Ka-band element, with both elements exhibiting field enhancement at 25 GHz.

The field distributions further show that the electromagnetic response is distributed across multiple interfaces rather than confined to a single interface or geometrical region. Specifically, the electric field hotspots near the metallic edges are consistent with surface charge accumulation and the associated electric response, whereas the magnetic-field localization

within the interlayer regions indicates a magnetic response associated with the current loops. Because adjacent metal–dielectric layers have gradually varied but comparable lateral dimensions, the field at a given frequency can extend across several neighboring layers. This multi-interface localization enables the incident wave to interact with multiple lossy regions and allows resonant regions with similar dimensions to contribute over adjacent frequency ranges.

Weak excitation of the K-band element remains visible at 30 GHz. The electric field exhibits an edge–center–edge distribution at an intermediate height, whereas the magnetic field forms two localized regions at another intermediate height. These secondary features are spatially distinct from the dominant hotspots in the Ka-band element, indicating that the K-band element retains a secondary response while the Ka-band element dominates at this frequency. Together with the absorption spectra, the frequency-dependent shift and coexistence of the localized electric and magnetic fields provide a physical explanation for the continuous K–Ka absorption band: the larger element primarily supports the low-frequency response, the smaller element dominates the high-frequency response, and their simultaneous responses near the band boundary help connect the two operating bands.

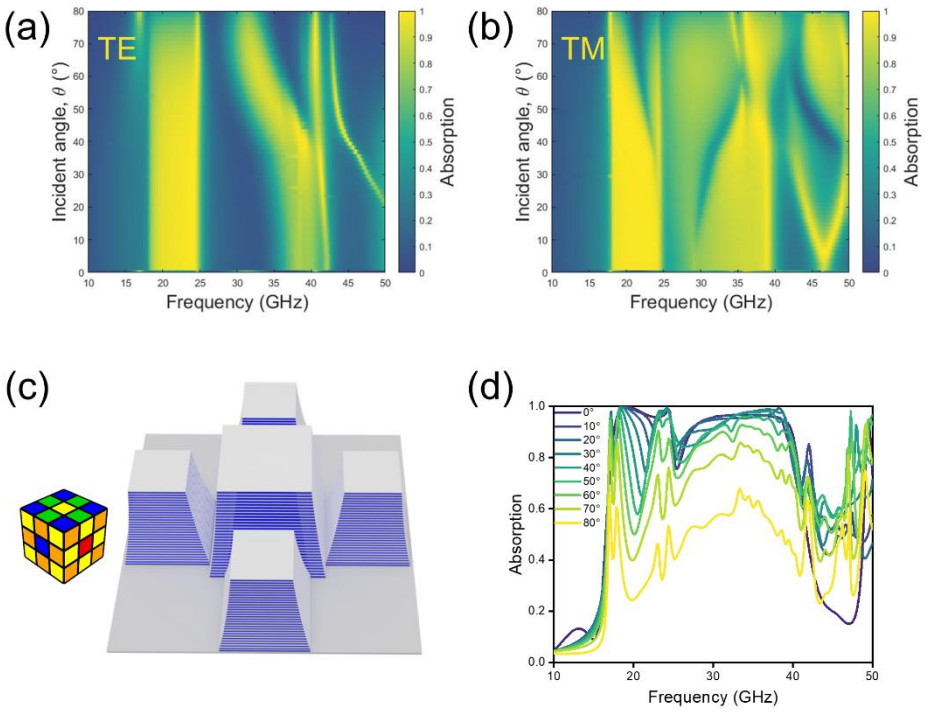

Figure 3. Polarization and angle-dependent absorption characteristics of the combined absorber before and after symmetry optimization. (a) Absorptance map of the K–Ka unit combination under TE-polarized incidence at different incidence angles. (b) Corresponding absorptance map under TM-polarized incidence. (c) Selected K-centered plus-pattern configuration. (d) Absorptance map of the selected configuration at different incidence angles.

To facilitate real-world applications, the effect of different oblique incident angles under different polarization angels is investigated and shown in Figure 3 (a) and (b). The angular response of the combined structure is examined under TE and TM polarized incidence by the incident angle parameter sweep from 0°to 80° in steps of 0.8° .The two polarizations exhibit clearly different angular dependences, demonstrating that the directional arrangement of the original K–Ka pair introduces polarization sensitivity.

As shown in the Figure 3 (a) and (b), the structure does not achieve stable broadband absorption spanning both the K and Ka bands under TE polarized incidence. In the K band, a > 80% absorption band exists from 18.1 to 24.8 GHz. According to the Equation (5), the relative absorption bandwidth is calculated to be 31%. In contrast, the absorption bandwidth in the Ka band is only 3.5 GHz. Nevertheless, the TE-polarized response shows strong wide-angle stability, with stable K-band absorption maintained over incidence angles from 0° to 70°. Under TM-polarized incidence, the structure exhibits better broadband absorption, with absorptance above 80% from 17.9 to 39.8 GHz and a relative absorption bandwidth of 76%. However, because the combined structure lacks x-y plane rotational symmetry, large oblique incidence angles affect energy dissipation within the dielectric layers. Consequently, the absorption bandwidth decreases slightly when the incidence angle exceeds 10° and decreases more substantially above 35°.

To reduce the polarization sensitivity and restore the structural symmetry, new symmetric unit configurations are designed. The Rubik's Cube provides an intuitive and elegant physical representation of mathematical group theory, with its structure and rotation rules exhibiting rich symmetry properties. Inspired by the face patterns encountered during the solution of a 3 × 3 × 3 Rubik's Cube, four symmetric configurations are developed: (a) a Ka-centered plus-pattern configuration, (b) a K-centered plus-pattern configuration, (c) a K-centered checkerboard-pattern configuration, and (d) a K-centered dot-pattern configuration. Their design schemes, based on the up face patterns of the corresponding Rubik's Cubes, and the resulting structural models are shown in left part of Figure S3 (a–d).

From the perspective of their two-dimensional arrangements, all four configurations exhibit the D_4 dihedral symmetry of a square according to group theory. Their unit distributions remain unchanged after a 90° rotation about the structural center or reflection about the *x*-axis, *y*-axis, or either diagonal. When the three-dimensional pyramidal geometry and substrate are taken into account, the four configurations belong to the C_{4v} point group in the Schoenflies point-group notation, possessing a fourfold rotation axis along the *z*-direction and four vertical mirror planes. This symmetry makes the *x*- and *y*-directions geometrically equivalent, providing a geometrical basis for similar responses to orthogonal polarizations under normal incidence.

Compare the four candidates's absorption performance, the (b) K-centered plus shape design consisting of one central K-band element and four surrounding Ka-band elements (shown in Figure 3 (c)) produces the most continuous broadband response, maintaining an absorption above 80% over 16–40 GHz(Shown in the 0° incident light in Figure 3 (d) and Figure S3).

The four configurations share the same D_4/C_{4v} symmetry but exhibit different absorption spectra. Therefore, rotational symmetry provides the geometrical basis for reducing polarization dependence, whereas the broadband response is further determined by the types, numbers, and positions of the K- and Ka-band elements. Configurations (a) and (b) have the same plus-pattern arrangement, but (b) possesses better direct K–Ka adjacencies while 4 K units in (a) do not close to center Ka unit enough. The weaker high-frequency response of configuration (a) indicates that the Ka-centered arrangement does not provide a sufficiently continuous Ka-band contribution. Configurations (b) and (c) contain the same numbers of K- and Ka-band elements, but the Ka-band elements are moved from the four sides to the four corners in configuration (c). The larger spectral fluctuations of configuration (c) indicate that direct side-by-side placement of dissimilar elements is more favorable for maintaining a continuous combined response. Configuration (d) contains four additional Ka-band elements compared with configuration (b), but this increase does not produce a corresponding improvement in absorption, showing that the number of resonators alone does not determine the broadband performance.

The K-centered plus-pattern configuration therefore combines fourfold rotational symmetry, an appropriate proportion of K- and Ka-band elements, and direct K–Ka adjacency along both in-plane directions. These features account for its smoother and more continuous absorption spectrum while retaining a relatively simple structure.

Figure 3(d) further evaluates the oblique-incidence response of the selected K-centered plus configuration and the corresponding results for all four topologies are provided in right part of Figure S3 (a-d). The optimized structure retains a comparatively high and continuous absorption response from normal incidence to approximately 50°. At 60°–80°, the absorptance decreases and the high-frequency response deteriorates more strongly than the low- and intermediate-frequency responses. Compared to Figure 3 (a) and (b), the new design significantly increases the stability to oblique incident light while maintaining wide range high absorption, further validating the effectiveness of the configuration optimization.

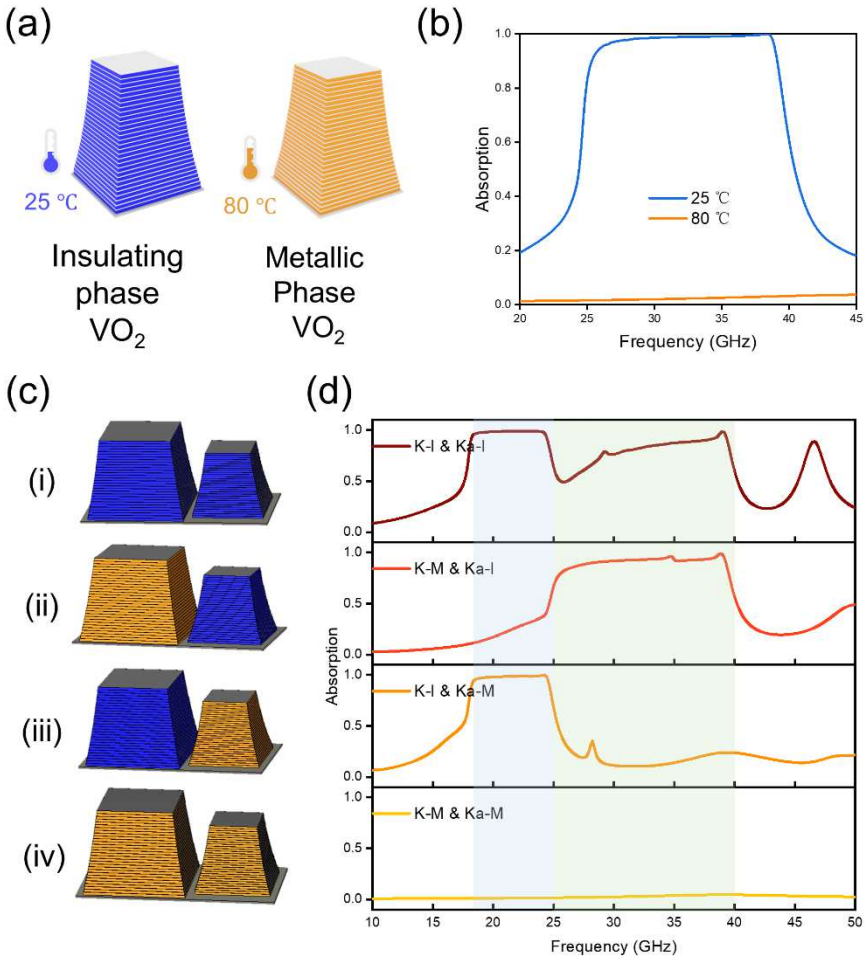

Figure 4. Thermally reconfigurable absorption characteristics of the nonlinear graded V–VO_2 hyperbolic absorber. (a) Schematics of the **Ka unit** with VO_2 in the insulating state at 25 °C and the metallic state at 80 °C. (b) Corresponding absorption spectra of the Ka unit. (c) Combined **K–Ka unit** with independently controlled VO_2 phase states. (d) Absorption spectra of the four types of K–Ka phase combinations.

VO_2 is a thermally driven phase-change material that behaves as an insulating at low temperature and undergoes an insulator-to-metal transition near 68°C [34]. For clarity, VO_2 is assumed to be in the insulating phase at 25 °C and in the metallic phase at 80 °C [26]. This transition produces substantial changes in its electrical conductivity and complex permittivity, which can be represented by temperature-dependent material parameters, commonly using a Drude model [30]. Incorporating VO_2 into a metamaterial absorber enables the absorber unit can consequently be switched from a passive, fixed-response device to a thermally reconfigurable platform.

Figure 4 (a) illustrates the proposed nonlinear graded V–VO_2 hyperbolic Ka absorber in the insulating state at 25°C and in the metallic state at 80°C. Its simulated absorption spectra are

compared in Figure 4 (b). In the insulating state, the element exhibits high absorption across most of the Ka band, with a broad plateau extending from 26 to 39 GHz. After VO_2 switches to the metallic state, the absorption is suppressed to only 3% over the same frequency range. The phase transition thus switches the unit between a broadband high-absorption state and a low-absorption state, providing the spectral contrast required for reconfigurable operation.

This switching mechanism is then extended to the combined K–Ka units shown in Figure 4 (c). When the phase of VO_2 in the K and Ka unit are set independently, four different absorption spectra are obtained. The four states correspond to (i) both elements insulating (K-I, Ka-I), (ii) the K element metallic and the Ka element insulating (K-M, Ka-I), (iii) the K element insulating and (iv) the Ka element metallic (K-I, Ka-M), and both elements metallic (K-M, Ka-M). Their absorption spectra are presented in Figure 4 (d) accordingly. These figures clearly show that the phase transitions of different structural elements produce distinct absorption responses in the K band (light-blue background) and Ka band (light-green background). Clear and observable differences are identified among the absorption spectra of the four states. Overall, the VO_2 phase transition enables both broadband absorption modulation and band-selective control of the individual elements. The two types of elements can be combined into the previously described plus configuration and periodically arranged to form a large-area VO_2-based dual-band metamaterial array. These distinguishable absorption states provide the basis for subsequent thermally controlled coding.

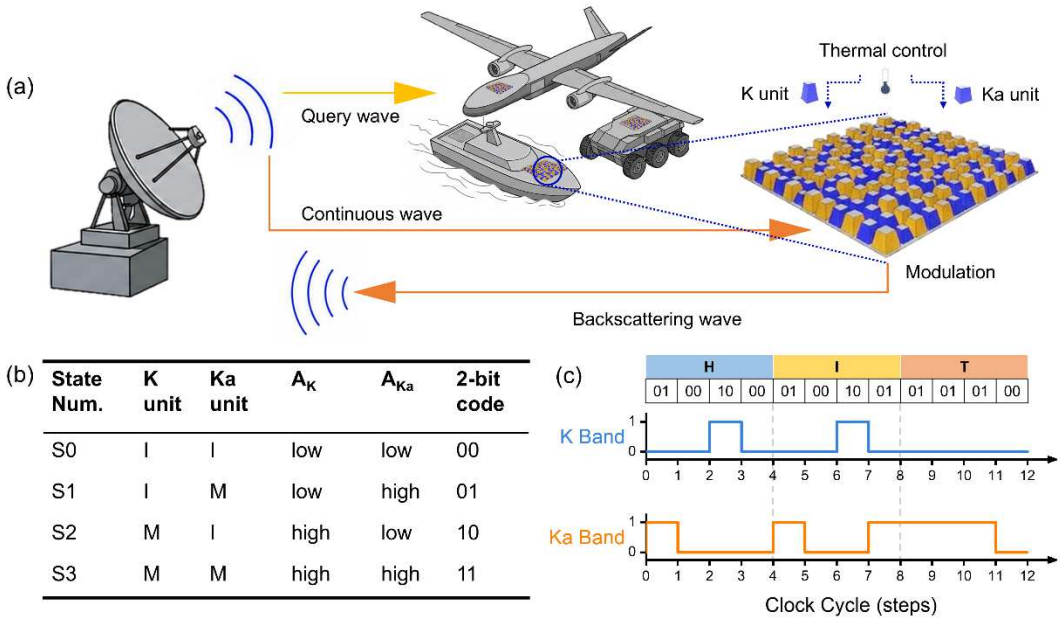

State Num.	K unit	Ka unit	A_K	A_{Ka}	2-bit code
S0	I	I	low	low	00
S1	I	M	low	high	01
S2	M	I	high	low	10
S3	M	M	high	high	11

Fig. 5. Operational principles and coding scheme of the VO_2-based dual-band metamaterial IFF system. (a) Schematic illustration of the end-to-end IFF across the friendly base-station radar to multiple tactical mobile platforms. (b)State mapping logic, and (c)Theoretical signal modulation profiles of the the ASCII-encoded payload "HIT".

By thermally inducing the phase transition of VO_2, the metamaterial array can be programmatically switched among four distinct absorption output states: (S0) K and Ka units both perform high absorption, (S1) K unit perform high absorption while Ka perform low, (S2) Ka unit perform high absorption n while K perform low and (S3) K and Ka unit both performs low absorption. This phase-switching ability enables a 2-bit modulator for the Identification Friend and Foe (IFF) becomes possible. The complete design frame work, including the comprehensive signal transmission pipeline, state mapping logic, and theoretical signal amplitude modulation dynamics of the proposed IFF system are summarized in Figure 5.

Figure 5 (a) presents how signal flows in the whole system. The proposed IFF protocol operates through a coordinated interrogation-response sequence. Initially, the friendly base-station radar emits a high-frequency pulse-modulated interrogation signal, termed the query wave. Upon receiving this query wave, the onboard receiver of the target platform decrypts and verifies the encoded authentication challenge using a pre-shared cryptographic key and algorithm. Once validated as a friendly request, the onboard cryptographic module generates a response command to actuate the internal thermal control units, which dynamically regulate the phase transitions of the **VO_2-based dual-band metamaterial array** coated on the platform surface. Subsequently, an unmodulated, single-frequency CW transmitted by the base station illuminates the target. The phase-change metamaterial array modulates the backscattered CW signal according to its dynamic state. Upon receiving the backscattered wave, the base station performs signal demodulation and decoding based on the State Mapping Table (Fig. 5b). Specifically, the temperature-dependent dielectric properties of VO_2 govern the optical states: temperatures $T < 68℃$ ($T > 68℃$) correspond to the insulating (metallic) phases of VO_2, yielding high-absorption (low-absorption) characteristics, respectively. Taking the S1 state as an example, the K units exhibit high absorption, resulting in a low received amplitude (A_K = low) at the base station; the Ka units exhibit low absorption, yielding a high received amplitude (A_{Ka} = high). By jointly detecting the spectral amplitudes across both K and Ka channels, the base station demodulates this distinct dual-channel signature (A_K=low, A_{Ka}=high) as the 2-bit logic sequence 01. The complete mapping logic for all states and their corresponding 2-bit digital codes are summarized in Figure 5 (b). Furthermore, using the signal "HIT" as demonstration, each 8-bit binary ASCII code is discretized into a sequence of four consecutive 2-bit symbol segments. These binary pairs sequentially drive the phase-change state transitions of the metamaterial in accordance with the pre-defined mapping logic, producing the theoretical signal amplitude modulation profiles shown in Figure 5 (c).

From an end-to-end IFF perspective, the proposed VO_2-based dual-band metamaterial array offers several advantages. Operating in a semi-passive backscatter mode, the system modulates the CW illumination emitted by the base station rather than generating active radio-frequency

signals locally. By eliminating the conventional active IFF transponders' need for dedicated high-power ratio-frequency transmitters and local oscillators, this reflective architecture fundamentally minimizes onboard energy consumption[35, 36]. Furthermore, the frequency-selective operation of the K- and Ka-band channels supports robust multi-band multiplexing. By exploiting the distinct spectral separation between the two bands, thermal modulation of one frequency range produces a negligible effect on the other, maintaining the integrity of the 2-bit state matrix (S0–S3). Based on the sharp contrast between the insulating and metallic phases of VO_2, the metamaterial exhibits a substantial amplitude difference between its high-reflection and high-absorption states. This pronounced amplitude distinction yields clear decision boundaries (A_K, A_{Ka}) at the receiver, ensuring reliable demodulation during the 12-step HIT ASCII-encoded data transmission. Consequently, this dual-band reflective architecture establishes a compelling strategy for integrating high-capacity backscatter authentication with dynamic radar stealth in tactical mobile platforms.

4. Conclusion

In this work, a thermally reconfigurable broadband microwave absorber based on nonlinearly graded V–VO_2 hyperbolic material is numerically demonstrated. The K- and Ka-units are first placed adjacent to extend the absorption band but this arrangement introduces polarization sensitivity. Rubik's-Cube-inspired symmetric configurations are subsequently developed, among which the K-centered plus configuration achieves absorptance above 80% over 16–40 GHz and maintains a stable broadband response for incidence angles from 0° to 50°. This improvement results from combining fourfold rotational symmetry with direct adjacency between the K- and Ka-band elements. Furthermore, the thermally induced phase transition of VO_2 enables independent control of the two types of units, producing four distinguishable absorption states and allowing the construction of a VO_2-based dual-band metamaterial array for thermally controlled coding. These results provide a new approach to broadband absorber design and demonstrate the potential for thermally controlled passive Identification Friend and Foe applications.

Reference

1. Petrov, V.M. and V.V. Gagulin, *Microwave absorbing materials.* INORGANIC MATERIALS, 2001. **37**(2): p. 93-98.
2. Yu, N. and F. Capasso, *Flat optics with designer metasurfaces.* Nat Mater, 2014. **13**(2): p. 139-50.
3. Landy, N.I., et al., *Perfect Metamaterial Absorber.* Physical Review Letters, 2008. **100**(20).
4. Cai, B., et al., *Ultra-broadband and wide-angle plasmonic light absorber based on all-dielectric gallium arsenide (GaAs) metasurface in visible and near-infrared region.* Results in Physics, 2024. **58**.
5. Xiao, C., et al., *Ultrabroadband and band-selective thermal meta-emitters by machine learning.* Nature, 2025. **643**(8070): p. 80-88.
6. Guo, T., et al., *Temperature Tunable Multiple Ultraviolet to Near-Infrared Perfect Absorption as Highly Sensitive Metamaterial Biosensor.* IEEE Sensors Journal, 2024. **24**(7): p. 9909-9915.
7. Cui, Y., et al., *Ultrabroadband light absorption by a sawtooth anisotropic metamaterial slab.* Nano Lett, 2012. **12**(3): p. 1443-7.
8. Ding, F., et al., *Ultra-broadband microwave metamaterial absorber.* Applied Physics Letters, 2012. **100**(10).
9. Zhou, J., et al., *Experiment and Theory of the Broadband Absorption by a Tapered Hyperbolic Metamaterial Array.* ACS Photonics, 2014. **1**(7): p. 618-624.
10. Yin, X., et al., *Ultra-wideband microwave absorber by connecting multiple absorption bands of two different-sized hyperbolic metamaterial waveguide arrays.* Sci Rep, 2015. **5**: p. 15367.
11. Fneish, Z., et al., *Curved Pyramidal Metamaterial Absorber: From Theory to an Ultra-Broadband Application in the [0.3 – 30] GHz Frequency Band.* Advances in Science, Technology and Engineering Systems Journal, 2021. **6**(2): p. 29-35.
12. Chen, H., et al., *Ultra-wideband microwave absorber based on multilayer patterned resistive film.* Materials Research Bulletin, 2024. **176**.
13. Ren, Z., et al., *A switchable terahertz metamaterial absorber between ultra-broadband and dual bands.* Frontiers in Physics, 2023. **11**.
14. Menon, A., et al. *An 18–26 GHz range calibrated linear synthetic aperture radar prototype suitable for security applications*. in *2018 IEEE 19th Wireless and Microwave Technology Conference (WAMICON)*. 2018.
15. Battaglia, A., et al., *Spaceborne Cloud and Precipitation Radars: Status, Challenges, and Ways Forward.* REVIEWS OF GEOPHYSICS, 2020. **58**(3).
16. Dai, J.Y., et al., *Wireless Communication Based on Information Metasurfaces.* IEEE Transactions on Microwave Theory and Techniques, 2021. **69**(3): p. 1493-1510.
17. Cui, T.J., et al., *Direct Transmission of Digital Message via Programmable Coding Metasurface.* Research (Wash D C), 2019. **2019**: p. 2584509.
18. Galati, G., et al., *The transponder data recorder: Implementation and first results.* IEEE Aerospace and Electronic Systems Magazine, 2014. **29**(2): p. 6-13.
19. Dhipu, T.M., V. Rishabh, and R. Rajesh, *Identification Friend or Foe Mode Code Detection Using Deep Pulse Detector Network.* Journal of Aerospace Information

Systems, 2022. **20**(1): p. 17-24.
20. Van Huynh, N., et al., *Ambient Backscatter Communications: A Contemporary Survey.* IEEE Communications Surveys & Tutorials, 2018. **20**(4): p. 2889-2922.
21. Herrojo, C., et al., *Chipless-RFID: A Review and Recent Developments.* Sensors (Basel), 2019. **19**(15).
22. Kimionis, J., A. Bletsas, and J.N. Sahalos, *Increased Range Bistatic Scatter Radio.* IEEE Transactions on Communications, 2014. **62**(3): p. 1091-1104.
23. Preradovic, S., et al., *Multiresonator-Based Chipless RFID System for Low-Cost Item Tracking.* IEEE Transactions on Microwave Theory and Techniques, 2009. **57**(5): p. 1411-1419.
24. Liu, H., J. Lu, and X.R. Wang, *Metamaterials based on the phase transition of VO(2).* Nanotechnology, 2018. **29**(2): p. 024002.
25. Kats, M.A., et al., *Ultra-thin perfect absorber employing a tunable phase change material.* Applied Physics Letters, 2012. **101**(22).
26. Lei, L., et al., *Tunable and scalable broadband metamaterial absorber involving VO2-based phase transition.* Photonics Research, 2019. **7**(7).
27. Zhang, W.W., et al., *Periodic trapezoidal VO(2)-Ge multilayer absorber for dynamic radiative cooling.* Opt Express, 2020. **28**(14): p. 20609-20623.
28. Schmid, S.W., et al., *Picosecond Femtojoule Resistive Switching in Nanoscale VO(2) Memristors.* ACS Nano, 2024. **18**(33): p. 21966-21974.
29. Li, C., et al., *Color-thermal multispectral camouflage with VO(2)-based dynamic regulator.* Light Sci Appl, 2025. **14**(1): p. 313.
30. Liu, D. and Z. Cui, *Broadband terahertz absorber based on patterned slotted vanadium dioxide.* Optical Materials, 2024. **152**.
31. Davidovich, M.V., *Hyperbolic metamaterials: production, properties, applications, and prospects.* Physics-Uspekhi, 2019. **62**(12): p. 1173-1207.
32. Wang, B.X., et al., *Review of Broadband Metamaterial Absorbers: From Principles, Design Strategies, and Tunable Properties to Functional Applications.* Advanced Functional Materials, 2023. **33**(14).
33. Nipun, M.K., et al., *From Narrowband to Wideband: A Review of Metamaterial Absorber Design and Development.* IUBAT Review, 2025. **8**(1): p. 145-175.
34. Wu, S.R., K.L. Lai, and C.M. Wang, *Passive temperature control based on a phase change metasurface.* Sci Rep, 2018. **8**(1): p. 7684.
35. Jia, X., et al., *Intelligent Reflecting Surface-Assisted Bistatic Backscatter Networks: Joint Beamforming and Reflection Design.* IEEE Transactions on Green Communications and Networking, 2022. **6**(2): p. 799-814.
36. Ma, H., et al., *Reconfigurable Intelligent Surface With Energy Harvesting Assisted Cooperative Ambient Backscatter Communications.* IEEE Wireless Communications Letters, 2022. **11**(6): p. 1283-1287.

Supplementary Files

This is a list of supplementary files associated with this preprint. Click to download.

- supplementaryinformation.docx